# NUMERICAL SIMULATION OF ALTERING THE RAW MEAL INLET POSITION IN A NOVEL SWIRL PRECALCINER

***Quanliang LI[1], Feng HE[2], Junlin XIE[2*], Shuxia MEI[1*], Chao ZHANG[3], Yuhua DENG[3]***

[1]School of Materials Science and Engineering, Wuhan University of Technology, Wuhan 430070, China

[2]Faculty of Materials and Manufacturing, Beijing University of Technology, Beijing 100124, China

[3]CBMI Construction Co., Ltd., Beijing 100176, China

[*] Corresponding authors; Junlin XIE: xjlclxy@126.com; Shuxia MEI: msx0303@163.com

*Conducted a numerical simulation to model a novel swirl precalciner, investigating how altering in the position of the raw meal inlet affects the internal gas flow, temperature field, and component concentration field within the precalciner. Applied the Realizable k-ε two-equation turbulent model to the continuous phase. For the particle phase (pulverized coal), employed the Discrete Particle Model and the discrete random walk model. Simulated the combustion of pulverized coal and the decomposition of calcium carbonate by using the Species Transport model combined with the Finite-Rate/Eddy-Dissipation model. Modeled the generation of $NO_x$ using a $NO_x$ model. The results show that, in comparison to the condition with four raw meal inlets, the six raw meal inlets condition has a better coupling of pulverized coal combustion and raw meal decomposition. The decomposition rate of raw meal has seen a slight improvement, and there is a significant improvement in the occurrence of localized high temperatures within the precalciner, resulting in a reduction of the outlet $NO_x$ concentration from 1251 ppm to 225 ppm.*

Key words*: precalciner, raw meal inlet position, pulverized coal combustion, calcium carbonate decomposition, $NO_x$, numerical simulation*

## 1. Introduction

In the cement industry, the precalciner, a central component of modern dry-process cement production technology, assumes a pivotal role in determining production capacity. Within the precalciner, the distribution of tertiary air and raw meal significantly affects the temperature, flow, and component concentration fields within the precalciner. Ensuring the uniform distribution of gas, coal and raw meal within the precalciner is essential for maintaining the stable operation of the precalciner. This facilitates rapid combustion of pulverized coal, enabling prompt absorption of the released heat by raw meal during calcium carbonate decomposition.

In recent years, as the greenhouse effect intensifies, reducing carbon emissions has become imperative for fostering the green and sustainable development of the cement industry [1, 2]. Within the silicate cement production process, approximately 40% of $CO_2$ emissions result from fuel combustion. This imposes greater demands on the energy-efficient operation of the precalciner.

Properly configuring the relative positions of the tertiary air inlet, pulverized coal inlet, and raw meal inlet is critical to ensuring the stable and efficient operation of the precalciner.

In the precalciner, the combustion of fuel and the reaction involving calcium carbonate decomposition are characterized by complexity, presenting significant challenges for experimental measurements and theoretical analyses. Consequently, many researchers have turned to numerical simulation technology to conduct a series of comprehensive investigations on decomposition furnaces [3–7]. In terms of optimizing the design of different types of calciner, Yang [8] carried out numerical simulations of the precalciner and investigated the effects of raw material angle, tertiary air velocity, and tertiary air temperature on NO concentration to find the optimal operating parameters of the precalciner. Wang [9] carried out numerical simulations of a TTF precalciner to comparatively study the effect of $CO_2$ atmosphere on the operation of the precalciner. It was found that the temperature distribution in the high-temperature region of the precalciner under $O_2/CO_2$ atmosphere was more uniform than that under $O_2/N_2$ atmosphere. However, the decomposition rate of the raw material decreased, and the process parameters must be improved to adapt to the $O_2/CO_2$ combustion technology. Mei [10] carried out numerical simulation of the vortex precalciner, analyzed the combustion characteristics of coal, explored the coupling mechanism of coal combustion and raw material decomposition, and provided important theoretical guidance for the optimization of the operating parameters of the decomposition furnace. In terms of energy conservation and emission reduction, Liu [11] performed numerical simulations of trinal-sprayed precalciner to investigate the effect of urea on the SNCR process at different injection heights, different injection flow rates, and different flow rates. The results show that different injection heights and different injection flow rates have a great influence on $NO_x$ removal efficiency and $NH_3$ escape, and stratified injection is recommended considering the cost-effectiveness. Zhang [12] et al studied the effects of ammonia spraying height, velocity, angle, ammonia-nitrogen ratio and other factors on the denitrification effect in TTF decomposition furnace on the basis of obtaining the internal flow and temperature fields of the decomposition furnace, and found the optimal scheme of denitrification. In terms of alternative fuel combustion, Gao [13] and Zhu [14] simulated the co-combustion processes of pulverized coal and biomass and pulverized coal and RDF in a TTF precalciner, and the results showed that a decreasing trend in the temperature, raw meal decomposition rate and $NO_x$ concentration of the decomposer with the increase of biomass fuels and RDF. Mikulčić H [15] simulated the co-combustion process of different types of pulverized coal and solid recovered fuels in the precalciner and found the maximum coal substitution rate allowed to be able to operate the decomposer stably.

In this paper, Fluent software was used to conduct numerical simulations of a new type of swirl-type precalciner. The study investigated the effects of raw meal injection positions on the flow field, temperature field, component concentration field, and $NO_x$ emissions. It provided an in-depth analysis of the interrelationships among gas, coal, and raw meal. This research has theoretical implications for energy conservation and carbon reduction in the precalciner.

## 2. Geometric model and mesh

Fig. 1 shows the geometric model and mesh of the swirl precalciner. The precalciner model features three types of inlets: gas inlets (flue gas, tertiary air), pulverized coal inlets, and raw meal inlets. Flue gas from the kiln tail enters the precalciner vertically from the bottom, while tertiary air enters tangentially from the side into the furnace. There are four pulverized coal inlets in total, with

two staged coal pipes located in the cone section (Coal1, Coal2), and two main coal pipes located near the tertiary air height (Coal3, Coal4). Six raw meal inlets are symmetrically distributed along the axis of the precalciner. For ease of subsequent analysis and discussion, the center of the flue gas inlet section is taken as the origin, and the upward vertical direction is defined as the positive y-axis. The overall height of the precalciner is approximately 70 m, with the volute part located at a height of 10-11.8 m. Regarding the grid division of the precalciner, tetrahedral meshing is used for the lower part of the precalciner, while hexahedral meshing is employed for the cylindrical part, resulting in a total of 1.28 million grids.

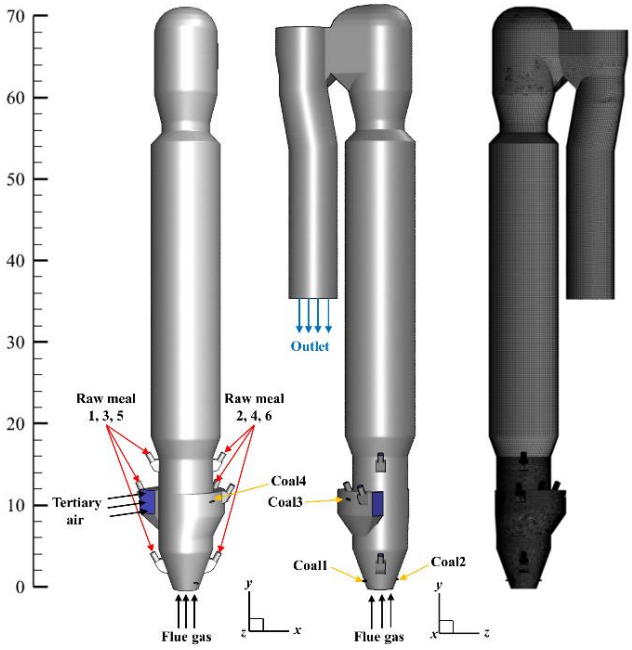


**Fig. 1 Geometric model and mesh of precalciner**

In the simulation process, in order to ensure the accuracy of the calculation, it is necessary to determine whether the simulation results change with the change of the number of grids, that is, to verify the grid independence. Fig. 2 shows the average temperature profile at the outlet of the precalciner for different number of grids. It can be found that when the number of girds is greater than 1.28 million, the average outlet temperature is basically unchanged, so this number of girds was used for calculation.

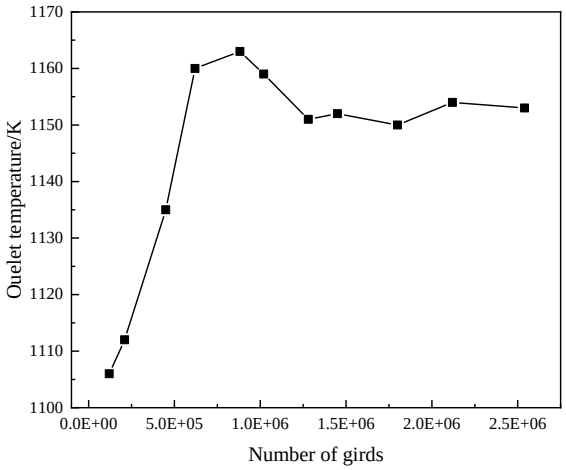


**Fig. 2 Mesh independence verification**

## 3. Mathematical model and numerical solution method

### 3.1. Mathematical model

The continuous phase (gas phase) are solved using the Realizable k-ε model [16] which has shown substantial improvements over the standard k-ε model, where the flow features include a strong streamline curvature, vortices, rotation, and recirculation [17–19]. The model is defined as:

$$\frac{\partial}{\partial t}(\rho k)+\frac{\partial}{\partial x_j}(\rho k u_j)=\frac{\partial}{\partial x_j}[(\mu+\frac{\mu_t}{\sigma_k})\frac{\partial k}{\partial x_j}]+G_k+G_b-\rho\varepsilon-Y_M+S_k \tag{1}$$

$$\frac{\partial}{\partial t}(\rho k)+\frac{\partial}{\partial x_j}(\rho\varepsilon u_j)=\frac{\partial}{\partial x_j}[(\mu+\frac{\mu_t}{\sigma_\varepsilon})\frac{\partial \varepsilon}{\partial x_j}]+\rho C_1 S\varepsilon-\rho C_2\frac{\varepsilon^2}{k+\sqrt{\nu\varepsilon}}+C_{1\varepsilon}\frac{\varepsilon}{k}C_{3\varepsilon}G_b+S_\varepsilon \tag{2}$$

$$C_1=\max[0.43,\frac{\eta}{\eta+5}],\eta=S\frac{k}{\varepsilon},S=\sqrt{2S_{ij}S_{ij}} \tag{3}$$

In these equations, $G_k$ represents the turbulence kinetic energy generation due to the mean velocity gradients. $G_b$ is the turbulence kinetic energy generation due to the buoyancy. $Y_M$ represents the contribution of the fluctuating dilatation in the compressible turbulence to the overall dissipation rate. $C_2$ and $C_{1\varepsilon}$ are constants. $\sigma_k$ and $\sigma_\varepsilon$ are the turbulent Prandtl numbers for k and ε, respectively. $S_k$ and $S_\varepsilon$ are user-defined source terms.

The movement trajectories of the particle phase are calculated using a Discrete Phase Model (DPM) and the discrete random walk model. It is assumed that the particles are spherical, and their diameter distribution follows the Rosin-Rammler distribution. Given that pulverized coal particles are dilute in the precalciner, interactions between pulverized coal are not considered.

For the combustion of pulverized coal and the decomposition of calcium carbonate, a Species Transport Model was utilized, coupled with a Finite-Rate/Eddy-Dissipation model for simulation. The pulverized coal combustion process consists of the release of volatiles, combustion of volatiles, and residual char combustion. The release of volatiles is modeled using a single-rate model. As for char combustion, a kinetics/diffusion-limited model is employed, considering that char reaction rate ($R_i$) is controlled by both kinetics and diffusion rates [20, 21]. The $R_i$ is defined as:

$$R_i = 4\pi r_p^2 P_{i.g} \frac{k_{diff,i} k_{kin,i}}{k_{diff,i} + k_{kin,i}} \quad (4)$$

The kinetic reaction rate of the char surface reaction($k_{kin,i}$) are in Arrhenius form:

$$k_{kin,i} = A_i T_p^{\beta_i} \exp(\frac{-E_i}{RT_p}) \quad (5)$$

Diffusion often controls the char-$O_2$ reaction rate at high temperature. The diffusion rate($k_{diff,i}$) can be expressed as:

$$k_{diff,i} = C_i \frac{[(T_p + T_\infty)/2]^{0.75}}{d_p} \quad (6)$$

Where $C_i$ is the overall mass diffusion-limited constant. In this paper, $A_i$ is 0.002, $E_i$ is $7.9\times10^7$ J/kmol, $C_i$ is $5.32\times10^{-12}$[22].

Regarding the decomposition of calcium carbonate, we consider the influence of the theoretical chemical reaction rate of calcium carbonate and the concentration of $CO_2$ on the actual decomposition rate [23]. The reaction rate of calcium carbonate in suspension in air follows the Arrhenius formula [24, 25]:

$$k = 2.5\times10^8 \exp(-\frac{2.05\times10^5}{RT}) \quad (7)$$

During the decomposition process, the combustion of pulverized coal and the flue gas from the kiln introduce a significant amount of $CO_2$. This $CO_2$ inhibits the release of $CO_2$ from within the calcium carbonate particles to the outside, thus affecting the decomposition rate. In order to realize the effect of $CO_2$ on the decomposition of calcium carbonate, it is necessary to consider the pressure difference of $CO_2$ between the inside and outside of the particles when calcium carbonate decomposes. The quantitative relationship between decomposition temperature and the equilibrium partial pressure of $CO_2$, $P_{CO2}$, as determined by Baker [26], is:

$$P_{co2} = 1.886\times10^{12} \exp(-\frac{19680}{T}) \quad (8)$$

The rate of the calcination reaction of calcium carbonate is proportional to the theoretical chemical reaction rate k and inversely proportional to the external $CO_2$ equilibrium pressure $P_g$ at the reaction interface. Therefore, the rate of the final calcination reaction can be expressed as:

$$k_{CaCO3} = -k \frac{(P_{CO2} - p_g)}{p_{CO2}} \quad (9)$$

A P-1 model is used to calculate radiative heat transfer [27]. The pollutant model was used to calculate the generation of $NO_x$ in the rotary kiln. Considering the generation of thermal $NO_x$ and fuel $NO_x$ in the rotary kiln, and $NO_x$ reduction by reburning, the model is set as follows:

(1) Thermal $NO_x$

The formation of thermal NOx is determined by a set of highly temperature-dependent chemical reactions known as the extended Zeldovich mechanism [28]. The principal reactions governing the formation of thermal $NO_x$ from molecular nitrogen are as follows:

$$O+N_2 \rightarrow NO+N \quad (10)$$

$$N+O_2 \rightarrow NO+O \quad (11)$$

(2) Fuel $NO_x$

For coal, fuel nitrogen is assumed to be distributed in volatiles and char, the reaction principle is shown in Fig. 3. Volatile nitrogen reacts at a certain temperature to form HCN and $NH_3$, one part

reacts with oxygen to form $NO_x$, and the other part reacts with the produced $NO_x$ to form $N_2$. For the remaining char N, it is assumed that it directly reacts with oxygen to generate $NO_x$, without intermediate products.

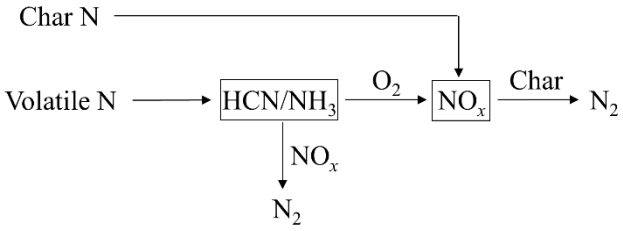


**Fig. 3 Fuel-$NO_x$ generation model**

### 3.2. Boundary conditions and numerical scheme

The precalciner is a newly designed 6000 t/d swirl precalciner. Due to the absence of actual operational data for reference at present, the operational parameters of an equally sized precalciner under actual working conditions are used as its boundary conditions. The mass flow rate of coal is 18.5 t/h, and the pulverized coal particle size distribution is between 70-200 μm, with equal mass flow rates for the four coal pipes. As for the raw meal inlet, the incoming raw meal to the precalciner is 400 t/h, with calcium carbonate accounting for approximately 80%. There are two methods for raw meal entry, referred to as case1 and case2, as shown in Fig. 4. Detailed boundary conditions for the precalciner are presented in Tab. 1. The composition of flue gas is provided in Tab. 2. Proximate analysis and ultimate analysis data of coal are presented in Tab. 3.

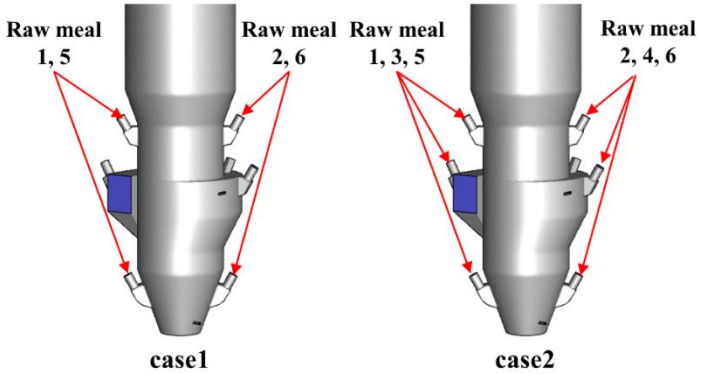


**Fig. 4 Schematic diagram of raw meal inlet location**

**Table 1. Boundary conditions**

| Boundary type | Temperature/K | Flow rate/kg·s$^{-1}$ | velocity/m·s$^{-1}$ |
|---|---|---|---|
| Flue gas | 1325 | - | 15 |
| Tertiary air | 1382 | - | 32.5 |
| Raw meal | 1023 | 88.88 | - |
| coal | 320 | 5.144 | 35 |

**Table 2. Composition of flue gas**

| Composition | Mole fraction/% |
|---|---|
| $O_2$ | 3.5 |
| $N_2$ | 79.04 |
| $CO_2$ | 17.36 |
| $NO_x$ | 0.1 |

**Table 3. Proximate analysis and ultimate analysis data of coal**

| Proximate analysis (ad)/% | | | | ultimate analysis (ad)/% | | | | | $Q_{gr}$/(kJ/kg) |
|---|---|---|---|---|---|---|---|---|---|
| M | A | V | FC | C | H | O | N | S | |
| 1.62 | 5.41 | 35.94 | 57.03 | 77.16 | 5.04 | 15.86 | 0.98 | 0.96 | 28500 |

The control equations of the fluid phase were discretized by the finite volume method. The difference equations were solved using a second-order upwind difference scheme. The pressure and velocity were coupled using Coupled algorithm. The Standard scheme was adopted for pressure discretization. The equations were numerically solved by the tridiagonal matrix algorithm (TDMA) method. The process was repeated until convergence was achieved with the convergence criterion being less than $10^{-6}$ for the energy and P-1 term, and less than $10^{-3}$ for the remaining residuals.

## 4. Results and discussion

### 4.1. Model verification

This paper introduces a novel swirl precalciner and employs the operational parameters of an equivalently sized precalciner as boundary conditions. Simulated data is compared to measurements from an equivalently sized precalciner, as showed in Table 4, to assess the simulation's validity and accuracy. Temperature measurements are derived from the cement plant's control room records, and exit gas composition data is collected through real tests using a flue gas analyzer. The table reveals that the simulated values exhibit a minimal margin of error when compared to actual production data, remaining well within the acceptable engineering error margin. Given the intricacies of coal powder combustion, chemical reactions in raw meal decomposition, and inherent numerical simulation errors, the comparative data suggests that the simulation results in this study are sound and faithfully represent the actual precalciner conditions.

**Table 4. Comparison of simulated and measured values**

| | Simulated values | Measures values | Relative error/% |
|---|---|---|---|
| Outlet temperature/K | 1151 | 1156 | 0.43% |
| $O_2$/% | 2.59 | 2.5 | 3.6% |
| $CO_2$/% | 32.17 | 33.3 | 3.39% |
| Decomposition rate% | 92.32 | 92-94% | - |

### 4.2. Gas flows

In the precalciner, appropriate gas flow streamlines are crucial for the stable operation of the precalciner. Comparing different positions for raw meal inlet reveals that raw meal throughout the

furnace is in a dilute phase, and varying inlet positions have essentially no effect on the trajectories of tertiary air and kiln gas. Therefore, we analyze four raw meal conditions (Case1) as examples.

Fig. 5 shows the streamline of tertiary air and kiln gas for the case1 condition. As shown in Fig. 5(a), tertiary air enters the precalciner diagonally from the side, creating a swirl at the volute section due to its tangential velocity. Influenced by vertically entering bottom flue gas, tertiary air spirals upward along the furnace wall. After reaching the top of the furnace, it continues to spiral downward and eventually escapes from the exit. In summary, due to the swirling effect at the volute section, the airflow has an extended residence time, with a maximum residence time of 18.6 s, effectively prolonging the residence time of pulverized coal and raw materials.

Fig. 5(b) shows the streamline of flue gas. The gas is observed moving vertically upward from the bottom. Under the influence of swirling tertiary air, the gas initiates an upward spiral along the central axis. When it reaches the top of the furnace, some of the gas experiences rebound, extending its residence time. Subsequently, the airflow spirals downward until reaching the exit. The maximum residence time for flue gas is approximately 19.7 s.

### 4.3. Comparison of coal combustion and temperature distribution

Fig. 6 shows the particle tracks of pulverized coal from two staged coal pipes, referred to as Coal1 and Coal2. As illustrated in the figure, upon the injection of pulverized coal into the precalciner, it undergoes significant influence from the flue gas. Consequently, the particles initiate an upward spiral motion along the central axis. As they traverse the volute section, certain particles experience deflection toward the furnace wall due to tangential velocity, thereby initiating a spiral motion along the wall, while others persist in their motion along the central axis. When the particles move to the top of the furnace, they gradually spiral downward, and the overall residence time of the particles is 9.6-14.2 s.

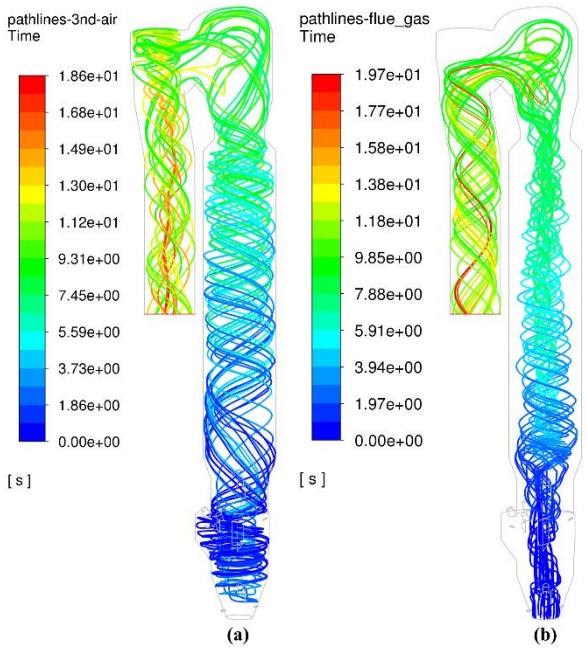


**Fig. 5 Streamline of tertiary air and flue gas (a)tertiary air (b)flue gas**

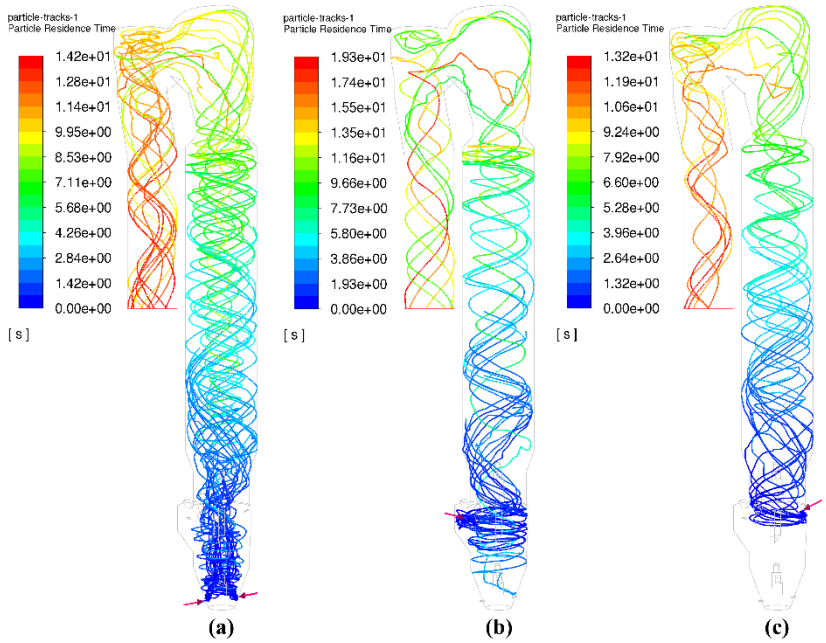


**Fig. 6 Pulverized coal particle tracks (a)Coal1 and Coal2, (b)Coal3, (c)Coal4**

Additionally, within the volute section, apart from the two staged coal pipes situated beneath the precalciner, two main coal pipe are present. One is positioned at the tertiary air inlet, referred as Coal3, while the other is located at the extremity of the volute, referred to as Coal4. Fig. 6(c) and Fig. 6(d) show the particle tracks of Coal3 and Coal4. Due to the arrangement of these two coal pipes along the path of tertiary air flow, the majority of particles spiral upward along the wall, while a smaller fraction initially descends before encountering the influence of the flue gas, subsequently prompting an ascent. Thanks to the distinctive volute structure, the residence time of Coal3 particles is significantly extended, reaching a maximum duration of 19.3 s. In contrast, Coal4 particles are injected at the volute's terminus, causing them to immediately spiral upward along with the tertiary air, resulting in a relatively shorter residence time, with a maximum of 13.2 s.

Upon entering the precalciner, pulverized coal experiences the rapid release and swift combustion of volatiles. Subsequently, char gradually begins to burn. To further investigate the combustion process of pulverized coal under different conditions, the release rate curves of volatile along the y direction are showed in Fig. 7. From Fig. 7, it can be observed that different conditions exhibit two peaks in the release rate of volatiles. However, due to variations in the position and mass flow rate of raw meal injection, the locations and rates of volatile release differ. In Case1 conditions, volatile rapidly releases at heights of 1 m and 11 m, while in Case2 conditions, it releases rapidly at heights of 2 m and 11 m. The release of volatiles from pulverized coal is swift and concentrated, occurring instantly upon entry into the precalciner. Notably, the release rates at y=1 m and y=2 m are lower than that at y=11 m, primarily due to lower temperatures at these position.

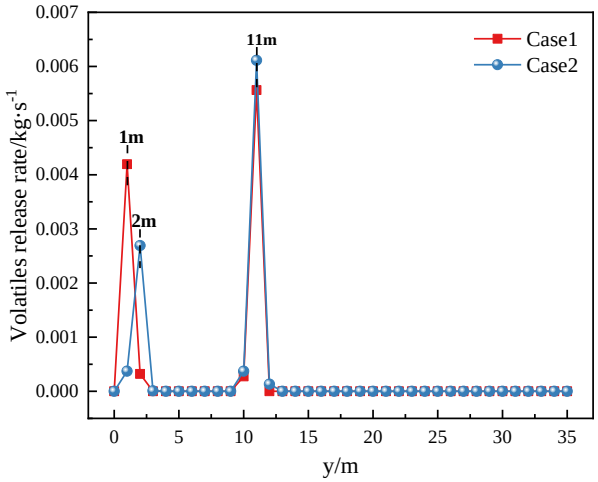


**Fig. 7 Volatile release rate curve along y direction**

Fig. 8 shows the combustion rate curves of volatile. Across different conditions, the combustion rates of volatiles exhibit similarity, featuring two peaks, both reaching their maximum at y=11 m. When comparing Case1 conditions to Case2 conditions, the volatiles combustion zone in the lower precalciner section shifts rearward in Case2. Within the range of 7 m ≤ y ≤ 11 m, volatile interacts with high-temperature tertiary air, inducing a rapid surge in combustion rates. With the large release of volatile matter from Coal3 and Coal4 pulverized coal at y=11 m (Fig. 7), the combustion rate reaches a peak, at which time the Case2 condition has a faster combustion rate. Beyond y=11 m, as the volatile content diminishes, combustion rates decrease swiftly, culminating in combustion completion around y=17 m, following a shorter combustion path.

During the combustion of volatiles, the combustion generates high-temperature heat, which subsequently ignites the char particles, initiating their combustion. Fig. 9 displays the combustion rate curves for char. Although combustion rates for char exhibit slight variations under different conditions, they consistently reach their peak at y=11 m. In comparison, char combustion under Case2 conditions exhibits greater uniformity and reduced susceptibility to localized high temperatures compared to Case1 conditions. Beyond the point of y=11 m, char combustion rates gradually decrease, ultimately completing combustion near y=50 m. The combustion duration for the pulverized coal is approximately 5.9 s.

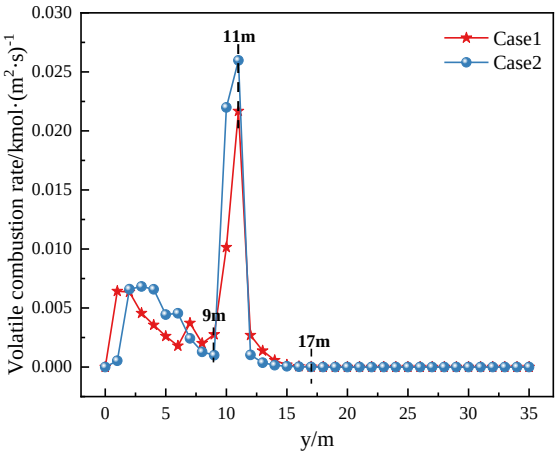


**Fig. 8 Volatile combustion rate curve along y-direction**

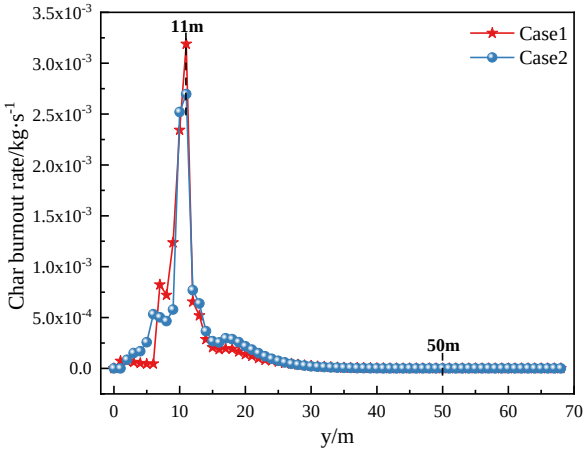


**Fig. 9 Char burnout rate curve along y-direction**

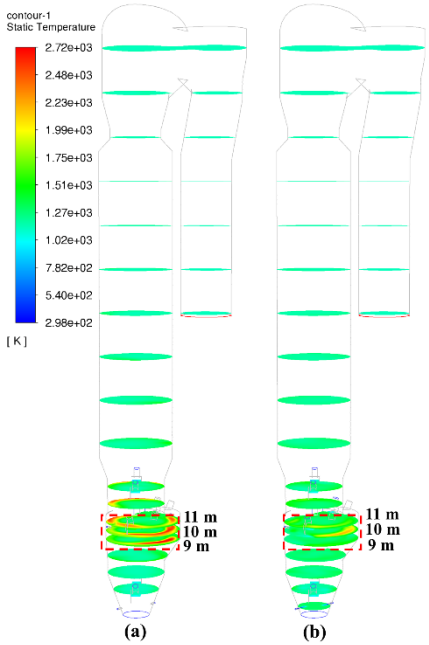


**Fig. 10 Contours of temperature for different height sections along the y direction (a)Case1 (b)Case2**

Fig. 10 and Fig. 11 show temperature contour and average temperature curves at various y-axis heights. Under Case1 conditions, combustion primarily concentrates in the volute section due to the influence of tertiary air on the trajectory of pulverized coal. However, the absence of raw meal injection in this region results in a limited coupling effect between the combustion of pulverized coal and the decomposition of raw meal. Consequently, significant localized high-temperature zones develop near the volute wall, reaching a maximum temperature of approximately 2750 K. Conversely, Case2 conditions benefit from the partial injection of raw meal in the volute, resulting in a more efficient coupling between the combustion of pulverized coal and the decomposition of raw meal. This leads to an overall uniform temperature field without notable localized high-temperature zones, and the highest recorded temperature is 2120 K. Variations in the positions of raw meal inlets between the two conditions account for the differences in the temperature field within the furnace. Nevertheless, despite similar total raw meal feeding and heat absorption, the outlet temperature from the precalciner remains consistent, at around 1151 K.

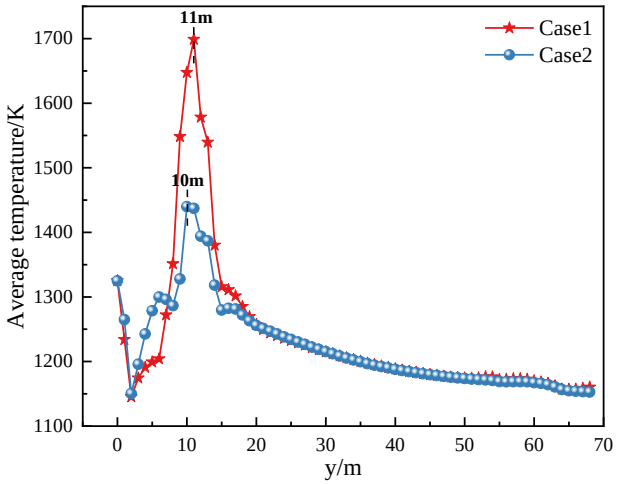


**Fig. 11 Comparison of average temperature curve along y direction**

### 4.4. Comparison of raw meal decomposition

To compare the decomposition of raw meal, contours of mole fraction of CaO at x=0 cross section were plotted under different conditions, as shown in Fig. 12. The figure reveals that, in general, as the lower portion of raw meal enters the precalciner from the cone section, influenced by high-temperature flue gas, a portion of $CaCO_3$ undergoes endothermic decomposition, forming CaO. As the raw meal ascends through the volute section, the rapid combustion of coal powder supplies additional heat, leading

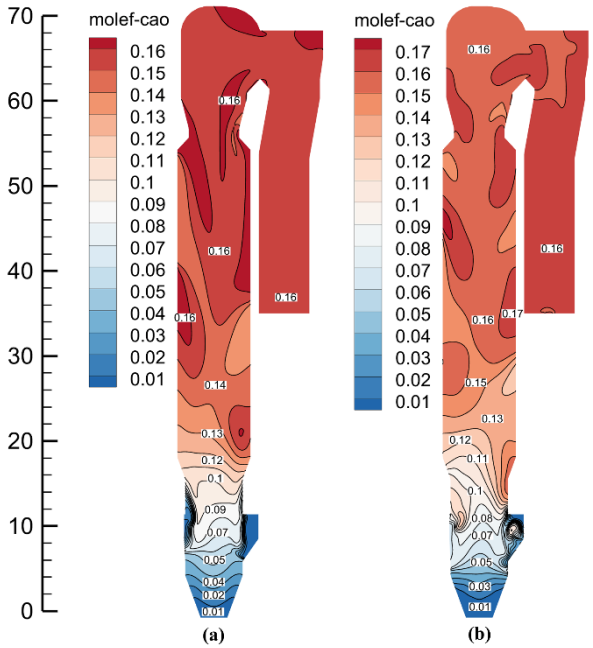


**Fig. 12 Contours of mole fraction of CaO at x=0 cross section (a)Case1 (b)Case2**

to the continuous decomposition of $CaCO_3$ into CaO. The upper two streams of raw meal come into contact with high-temperature gas as they enter the precalciner, initiating the rapid decomposition of $CaCO_3$. As the raw meal progresses to the upper half of the precalciner, the majority of $CaCO_3$ is nearly fully decomposed, and the CaO concentration remains stable. A comparison between Fig. 12(a) and Fig. 12(b) reveals that, in the Case2 condition, the change in CaO molar fraction is more uniform.

Whereas in the Case2 condition, the reaction is concentrated, with $CaCO_3$ primarily reacting in the lower and middle sections.

To conduct a more in-depth analysis of raw meal decomposition in the precalciner, average mole fraction of $CaCO_3$ and CaO along y direction were plotted for both conditions, as depicted in Fig. 13. In general, the behavior of $CaCO_3$ decomposition varies between the two conditions. Under the Case2 condition, the primary raw meal decomposition takes place near y=10 m, in the vicinity of the volute section. Compared with the Case1 condition, the Case2 condition has a more uniform decomposition rate, better coupling of pulverized coal combustion and raw material decomposition, and can effectively reduce the local high temperature (Fig. 12). Calculations indicate that the decomposition rate for the condition with four raw meal inlets is approximately 92.32%, whereas for the condition with six raw meal inlets, it is 93%, slightly higher.

In conclusion, it is evident that in the condition with six raw meal inlets, there is improved coupling between the combustion of coal powder and the decomposition of raw meal, resulting in the avoidance of significant localized high-temperature zones. Nonetheless, in the condition with six raw meal inlets, some localized high-temperature regions persist around y=10 m.

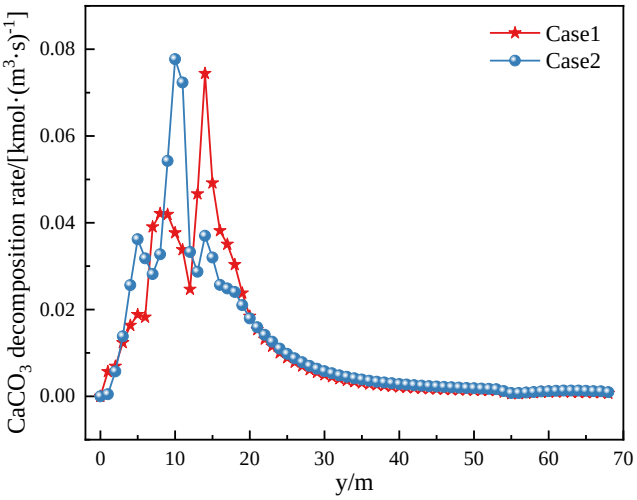


**Fig. 13 Comparison of average mole fraction of $CaCO_3$ and CaO along y direction for different working conditions**

### 4.5. Comparison of $NO_x$

Regarding $NO_x$ generation in the precalciner, it's essential to consider two types: thermal $NO_x$, which results from localized high temperatures in the furnace, and fuel $NO_x$, produced during the combustion of pulverized coal. Fig. 14 displays the average mole fraction of $NO_x$ curve along the y direction under different conditions. From the figure, it can be observed that in the Case1 condition, the precalciner exist localized high-temperature zones due to the relatively poor coupling between pulverized coal combustion and raw meal decomposition. As a result, there is a higher concentration of thermal $NO_x$ in the precalciner, leading to an outlet $NO_x$ volume concentration of 1251 ppm. Transitioning to Case2 conditions reduces these high-temperature zones and the maximum temperature, shifting the primary $NO_x$ type to fuel $NO_x$. Calculations show that the outlet $NO_x$ volume concentration under Case2 is significantly lower at 225 ppm, indicating a substantial reduction in $NO_x$ emissions compared to Case1.

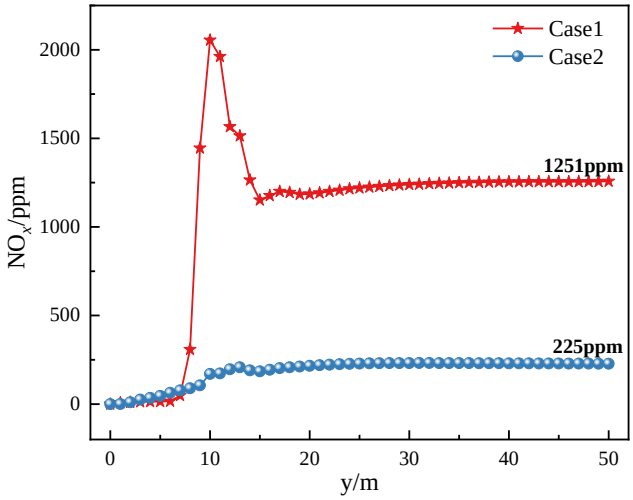


**Fig. 14 Average mole fraction of $NO_x$ curve along the y direction**

## 5. Conclusion

A numerical simulation was conducted to model a novel swirling precalciner, investigating the impact of variations in raw meal inlet positions on the internal flow field, temperature distribution, $CaCO_3$ decomposition process, and $NO_x$ generation. The following conclusions were drawn:

(1) In this precalciner, the bottom flue gas moves vertically upward. Upon encountering the tertiary air entering diagonally from the side, it initiates a spiral ascent along the central axis of the precalciner.

(2) In the precalciner, the primary combustion zone for pulverized coal is located near the volute section, achieving a 100% burnout rate. Compared to the four raw meal inlet condition, the six raw meal inlet condition results in a more uniform pulverized coal combustion, reducing the likelihood of localized high-temperature zones.

(3) In the condition of four raw meal inlets, a greater amount of $CaCO_3$ decomposition takes place in the conical section. However, due to the absence of a raw meal inlet at the volute in this condition, there is a relatively poor coupling between pulverized coal combustion and raw meal decomposition. This results in the formation of extensive localized high-temperature zones along the wall. The final decomposition rate for this condition is 92.32%.

(4) In the case of six raw meal inlets, two streams of raw meal are injected at the volute. This configuration leads to a better coupling between pulverized coal combustion and raw meal decomposition, avoiding the generation of extensive localized high-temperature zones. The final decomposition rate is 93%, slightly higher than that of the four raw meal inlet condition.

(5) The four raw meal inlet condition, influenced by localized high temperatures, generates high-concentration localized $NO_x$ at the volute. The resulting $NO_x$ concentration at the outlet is 1251 ppm. In contrast, the six raw meal condition exhibits no significant localized high temperatures and primarily generates fuel $NO_x$. The outlet $NO_x$ concentration is 234 ppm, significantly lower than the four raw meal inlet condition.

In summary, the six raw meal inlet condition outperforms the four raw meal inlet condition.

**Acknowledgment**

This work was financially supported by the Oxy-fuel Combustion Technology R&D of CBMI Construction Co., Ltd. (CBMI-KJCX-2021-04)

**Nomenclature**

| | |
|---|---|
| ***Acronyms*** | |
| A | Ash |
| FC | Fixed carbon |
| M | Moisture |
| V | Volatile |
| ***Variable or parameter*** | |
| $A_i$ | Pre-exponential factor [$s^{-1}$] |
| $C_{1\varepsilon}$ | Constant [-] |
| $C_2$ | Constant [-] |
| $C_i$ | Mass diffusion-limited constant [-] |
| $d_p$ | Particle diameter [$m$] |
| $E_i$ | Activation energy [$J/kmol$] |
| $G_b$ | The generation of turbulence kinetic energy due to buoyancy [$J$] |
| $G_k$ | The generation of turbulence kinetic energy due to the mean velocity gradients [$J$] |
| k | Turbulent kinetic energy [$J$] |
| $k_{CaCO3}$ | Calcium carbonate reaction rate [$kmol \cdot m^{-3} \cdot s^{-1}$] |
| $k_{diff,i}$ | Kinetic limited reaction rate [$kmol \cdot m^{-3} \cdot s^{-1}$] |
| $k_{kin,i}$ | Diffusion limited reaction rate [$kmol \cdot m^{-3} \cdot s^{-1}$] |
| $P_{CO2}$ | Internal CO2 pressure [$Pa$] |
| $P_g$ | External $CO_2$ pressure [$Pa$] |
| $P_{i,g}$ | Partial pressure of oxidant species in the gas surrounding the combusting particle [$Pa$] |
| $R_i$ | Rate of particle surface reaction [$kg \cdot s^{-1}$] |
| R | Molar gas constant [$J \cdot mol^{-1} \cdot K^{-1}$] |
| $r_p$ | Particle radius [$m$] |
| $S_k$ | User-defined source terms [-] |
| $S_\varepsilon$ | User-defined source terms [-] |
| $T_p$ | Particle temperature [$K$] |
| $T_\infty$ | Surrounding gas temperature [$K$] |
| $u_j$ | Gas velocity [$m \cdot s^{-1}$] |
| $Y_M$ | The dilatation dissipation term [-] |
| ***Greek letters*** | |
| $\beta_i$ | Temperature exponent [-] |
| $\delta_k$ | Turbulent Prandtl numbers for k [-] |
| $\delta_\varepsilon$ | Turbulent Prandtl numbers for ε [-] |
| $\varepsilon$ | Turbulent dissipation rate [%] |
| $\mu_t$ | Eddy viscosity [$Pa \cdot s$] |

| | |
|---|---|
| ρ | Gas density [$kg \cdot m^{-3}$] |

**References**


[1] Guo, Y., et al., A Review of Low-Carbon Technologies and Projects for The Global Cement Industry, *J. Environ. Sci.*, *136* (2024), pp. 682-697

[2] Dinga, C.D., Wen, Z., China's Green Deal: Can China's Cement Industry Achieve Carbon Neutral Emissions By 2060?, *Renew. Sustain. Energy Rev.*, *155* (2022), pp. 111931

[3] Li, D., et al., Experimental Study and CFD Modeling of $NO_x$ Reduction and Reductive Gas Formation in Deep Reburning of Cement Precalciner, *Fuel Process. Technol.*, *229* (2022), pp. 107183

[4] Sharma, P., et al., Aspen Plus Simulation of an Inline Calciner for White Cement Production with A Fuel Mix of Petcoke and Producer Gas, *Energy*, *282* (2023), pp. 128892

[5] Zhang, L., et al., Numerical Simulation of Oxy-Fuel Combustion with Different $O_2/CO_2$ Fractions in a Large Cement Precalciner, *Energy Fuels*, *34* (2020), 4, pp. 4949-4957

[6] Nakhaei, M., et al., CPFD Simulation of Petcoke and SRF Co–Firing in a Full–Scale Cement Calciner, *Fuel Process. Technol.*, *196* (2019), pp. 106153

[7] Wang, B., Kao, H., Numerical Simulation of $O_2/CO_2$ Combustion in Decomposition Furnace, *Therm. Sci.*, (2023), 00, pp. 73-73

[8] Yang, Y., et al., Numerical Simulation of Low Nitrogen Oxides Emissions Through Cement Precalciner Structure and Parameter Optimization, *Chemosphere*, *258* (2020), pp. 127420

[9] Wang, B., Kao, H., Numerical Simulation of $O_2/CO_2$ Combustion in Decomposition Furnace, *Therm. Sci.*, *27* (2023), 5 Part B, pp. 4307-4320

[10] Mei, S., et al., Numerical Simulation of the Complex Thermal Processes in a Vortexing Precalciner, *Appl. Therm. Eng.*, *125* (2017), pp. 652-661

[11] Liu, Y., Kao, H., Numerical Simulation of Urea Based SNCR Process in a Trinal-Sprayed Precalciner, *J. Renew. Mater.*, *9* (2021), 2, pp. 269

[12] Zhang, L., et al., Numerical Simulation of SNCR Denitration in Cement Precalciner, *J. USST.*, *41* (2019), 1, pp. 14-21(in Chinese)

[13] Gao, R., et al., Numerical Simulation of Co-Combustion of Pulverized Coal and Biomass in TTF Precalciner, *Fuel*, *334* (2023), pp. 126515

[14] Zhu, J., Kao, H., Numerical Simulation of Co-Combustion of Pulverized Coal and Different Proportions of Refused Derived Fuel in TTF Precalciner, *J. Renew. Mater.*, *9* (2021), 7, pp. 1329-1343

[15] Mikulčić, H., et al., Numerical Evaluation of Different Pulverized Coal and Solid Recovered Fuel Co-Firing Modes Inside a Large-Scale Cement Calciner, *Appl. Energy*, *184* (2016), pp. 1292-1305

[16] Shih, T.-H., et al., A New K-epsilon Eddy Viscosity Model for High Reynolds Number Turbulent Flows: Model Development and Validation, Report No. CMOTT-94-6, August 1, 1994

[17] Rohdin, P., Moshfegh, B., Numerical Predictions of Indoor Climate in Large Industrial Premises. A Comparison Between Different K–ε Models Supported by Field Measurements, *Build. Environ.*, *42* (2007), 11, pp. 3872-3882

[18] Lateb, M., et al., Comparison of Various Types of K–ε Models for Pollutant Emissions Around a Two-Building Configuration, *J. Wind Eng. Ind. Aerodyn.*, *115* (2013), pp. 9-21

[19] Shaheed, R., et al., A Comparison of Standard K–ε and Realizable K–ε Turbulence Models in Curved and Confluent Channels, *Environ. Fluid Mech.*, *19* (2019), 2, pp. 543-568

[20] BAUM, M.M., STREET, P.J., Predicting The Combustion Behaviour of Coal Particles, *Combust. Sci. Technol.*, *3* (1971), 5, pp. 231-243

[21] Field, M.A., Rate of Combustion of Size-Graded Fractions of Char from a Low-Rank Coal Between 1 200°K and 2 000°K, *Combust. Flame*, *13* (1969), 3, pp. 237-252

[22] Toporov, D., et al., Detailed Investigation of a Pulverized Fuel Swirl Flame in $CO_2/O_2$ Atmosphere, *Combust. Flame*, *155* (2008), 4, pp. 605-618

[23] Mao, Y., et al., Numerical Modelling of Multiphase Flow and Calcination Process in an Industrial Calciner with Fuel of Heavy Oil, *Powder Technol.*, *363* (2020), pp. 387-397

[24] Hu, N., Scaroni, A.W., Calcination of Pulverized Limestone Particles Under Furnace Injection Conditions, *Fuel*, *75* (1996), 2, pp. 177-186

[25] Borgwardt, R.H., Calcination Kinetics and Surface Area of Dispersed Limestone Particles, *AIChE J.*, *31* (1985), 1, pp. 103-111

[26] Baker, E.H., 87. The Calcium Oxide–Carbon Dioxide System in The Pressure Range 1—300 Atmospheres, *J Chem Soc*, *0* (1962), 0, pp. 464-470

[27] CHENG, P., Two-Dimensional Radiating Gas Flow by a Moment Method, *AIAA J.*, *2* (1964), 9, pp. 1662-1664

[28] Zeldvich, Y.B., The Oxidation of Nitrogen in Combustion and Explosions, *J Acta Physicochim.*, *21* (1946), pp. 577

Received: 09.11.2023.
Revised: 01.03.2024.
Accepted: 07.03.2024.